Microstructural insights into EUROFER97 batch 3 steels

Michael Duerrschnabel [*], Ute Jäntsch, Ramil Gaisin, Michael Rieth

Institute of Applied Materials, Karlsruhe Institute of Technology, Hermann-von-Helmholtz-Platz 1, D-76344 Eggenstein-Leopoldshafen, Germany

A B S T R A C T

Extensive analytical electron microscopical analyses were carried out from the micrometer scale down to the nanometer scale to characterize three variants of the 9% reduced activation ferritic martensitic (RAFM) steel EUROFER97/3. No huge microstructural differences were observed between the three grades. Electron back-scatter diffraction (EBSD) in a scanning electron microscope (SEM) was used to determine prior austenite grain (PAG) and lath sizes of the martensite matrix. The PAG size varied between 4.5 μm and 6.5 μm depending on the reconstruction algorithm. Furthermore, the martensitic lath sizes determined by SEM-EBSD are only half or 1/3 of that determined manually from transmission electron microscopy (TEM) images, which might be related to the limited statistics in this type of TEM data evaluations. The SEM-EDX shows that $M_{23}C_6$-type phases are preferentially located on lath and grain boundaries due to preferential diffusion of elements like Cr, W, and C to and along grain boundaries, which agrees with TEM-EDX measurements. TEM techniques like STEM-EDX and high-resolution TEM were used to describe the occurring precipitates i.e., $M_{23}C_6$, VN, TaC morphologically, structurally, and chemically. In addition, the thermodynamic calculations were carried out to explain phase formation, phase fraction and phase composition. The results are in good agreement with the experimentally determined values. These results will provide a profound basis to explain the mechanical performance of these materials. Furthermore, it will lay a good reference basis of comparison for the material after neutron irradiation.

Introduction

Future fusion reactors require large amounts i.e., 1000 tons or more of high-performance structural materials. 9wt.%Cr reduced activation ferritic-martensitic (RAFM) steels are excellent candidates fulfilling these requirements, since they can be produced in the necessary amounts and their operational performance window lies in the temperature range of 350–550 °C [1]. For operation temperatures exceeding this limit oxide-dispersion strengthened (ODS) steels are the structural material of choice in a nuclear environment [2]. However, their amount of material production is still limited to a low kilogram range and their incorporation into functional devices is a current research topic [3–5]. EUROFER97 is the European RAFM version, whose development begun more than 25 years ago by replacing radiologically undesired elements like Mo, Nb, Ni and Co by their lower-activation counterparts like Ta, W, Mn, and V. Furthermore, impurity elements like for example Al, Ag, Zn etc. need to be limited to keep the low-level waste criteria down at a few hundred years [6,7]. Since then, a continuous material and fabrication development and qualification process for EUROFER as structural material for fusion power plants is carried out [8]. An extensive review on

EUROFER, its development history and its technological relevance for fusion applications is given by Rieth et al. [5]. The latest EUROFER specification is EUROFER97/3, which will be analyzed micro-structurally in the following. The addition of about 0.2 wt% of V improves creep strength and impact behavior [9], whereas about 1 wt% of W is added as solution strengthening element. The influence of this elemental exchange on the microstructure, the mechanical properties, and the neutron irradiation behavior was and still is a subject in materials research within the nuclear fusion community. The neutron irradiation influence on microstructure of previous EUROFER variants is for example studied by Dethloff et al. [10,11] and Klimenkov et al. [12–14].

For a complete understanding of the material behavior, it is necessary to characterize the material at different length scales. Mechanical tests typically use samples of several centimeters or millimeters in size, whereas the microstructural characterizations are typically in the micro- and nanometer range. Ferritic-martensitic steels have a typical microstructure consisting of PAG subdivided by martensitic laths that can be arranged in several packages within one PAG. As shown for example by Hoffmann et al. [15] a good way to unravel this structure is to make use of scanning electron microscopy (SEM) and electron backscattering

diffraction (EBSD).

Another important factor for many high-temperature applications is the presence and spatial distribution of nanoscale precipitates inside the steel matrix. The formation of those precipitates depends on the thermal treatment and on the overall composition. Unraveling the microstructure and nanochemistry of reduced-activation ferritic martensitic and related steels is usually conducted via atom probe tomography (APT) [16,17] and/or TEM [18–20]. In case of EUROFER97 two main fractions of precipitates are observed using transmission electron microscopy (TEM) [21–23]: (a) coarse $M_{23}C_6$-type carbides and (b) fine MX-type precipitates. The $M_{23}C_6$-type precipitates have a typical average size of 100–200 nm, whereas the MX-type precipitates are about one order of magnitude smaller than the $M_{23}C_6$ precipitates. Chemical characterization on the nanometer scale of EUROFER97 batch 1 was carried out by Klimenkov et al. [18]. It was found by Klimenkov et al. [18] that the $M_{23}C_6$ are mainly Fe/Cr carbides with small amounts of V and W. Furthermore, it was found that the MX-type precipitates divide into two fractions: (i) TaC and (ii) VN. Multivariate statistical analyses for example of STEM-EDX datasets can be used for denoising purposes or can help with their interpretation. An overview of the method, different algorithms and its impact on hyperspectral datasets in electron microscopy are for example described in [24,25]. Morphological precipitate analyses carried out by Fernandez et al. [21] showed that both the $M_{23}C_6$- and MX-type precipitates follow a log-normal size distribution. It is also known that $M_{23}C_6$-type precipitates are preferentially located at lath or PAG boundaries, whereas the MX-type precipitates can also be present everywhere in the volume. The role of both types of precipitates is to stabilize the microstructure by pinning lath or grain boundaries or dislocations, which improves the mechanical properties and extends the operation temperature window of the material to higher temperatures.

In this study, two grades of 9 wt.%Cr EUROFER97/3 alloys were produced with small variations in chemical composition to compare them to an industrial grade of EUROFER97/3. The aim is to simplify the chemical composition while retaining the mechanical properties of earlier EUROFER97 grades. The compositional simplification intends to facilitate the industrial scale-up. The present study focuses on the microstructural characterization of the material by SEM and TEM to lay the base for future aging and irradiation studies, which are currently ongoing. These analyses include the determination of precipitates' number densities, size distribution and morphology as well as the determination of lath and PAG sizes.

Experimental

Three EUROFER97/3 steels are microstructurally characterized within this work. In the following AQ ad AC denote air quench and air cooling, respectively.

1. EF3i: Industrial grade EUROFER97/3 heat treated with 980 °C/38 min + AQ + 760 °C/145 min + AC
2. EF3: In-house made EUROFER97/3 batch heat treated with 980 °C/30 min + AQ + 780 °C/120 min + AC
3. EF3s: In-house made chemically simplified EUROFER97/3 batch heat treated with 980 °C/30 min + AQ + 780 °C/120 min + AC

Their chemical composition in wt% is summarized in Table 1.

SEM and EBSD have been carried out in a Zeiss Merlin and in a Zeiss Auriga, both equipped with an EDAX Hikkari high speed EBSD camera. SEM samples have been first mechanically polished followed by an electropolishing step. Finally, the surface has been cleaned by Ar polishing in a JEOL cross section polisher. The EBSD maps were measured at 20 kV with a beam current of 10 nA and a step size of 80 nm. Points with a confidence index (CI) lower than 0.1 were discarded from the maps.

For the TEM investigations disks of 0.15 mm thickness and 3 mm diameter have been fabricated by mechanical polishing and punching. Electrochemical thinning was performed using a Tenupol-3 jet polisher with a 20% H_2SO_4 80% CH_3OH solution as electrolyte at a voltage of 10–12 V at 23 °C.

The nanoscale of the materials was investigated using a Thermofisher Talos F200X scanning transmission electron microscope (STEM) equipped with a SuperX energy-dispersive X-ray detection system as well as with a Gatan Enfinium electron energy-loss spectroscope. The microscope was operated at 200 kV acceleration voltage. TEM data evaluation was carried out using Digital Micrograph™, Imagej, Hyperspy [26] and SingleCrystal [27] softwares.

Thermodynamic calculations have been carried out using the ThermoCalc software version 2021a. For all calculations the TCFE7 and MOBFE2 libraries were used to include all necessary RAFM steel elements. For simplicity the system size and pressure were fixed to 1 mol and 1000 hPa, respectively. For the calculations elements with concentrations <0.0001 wt% have been neglected.

Table 1
Chemical composition of the 3 EUOFER97/3-type steels.

Element	Concentration [wt%] EF3i			Concentration [wt%] EF3			Concentration [wt%] EF3s		
C	0.0950	±	0.0046	0.0941	±	0.0079	0.0791	±	0.0066
Al	0.0033	±	0.0006	<0.0010	±	–	<0.0010	±	–
B	0.0008	±	0.0001	–	±	–	–	±	–
Co	0.0030	±	0.0000	–	±	–	–	±	–
Cr	8.8133	±	0.0058	9.2500	±	0.1600	9.2900	±	0.1600
Cu	0.0030	±	0.0000	0.0069	±	0.0003	0.0055	±	0.0002
Fe	Bal.	±	–	Bal.	±	–	Bal.	±	–
Mn	0.5433	±	0.0058	0.4950	±	0.0090	0.0163	±	0.0003
Mo	0.0020	±	0.0000	0.0024	±	0.0001	0.0394	±	0.0011
N	0.0367	±	0.0040	0.0409	±	0.0087	0.0265	±	0.0056
Nb	0.0020	±	0.0000	0.0003	±	–	0.0002	±	–
Ni	0.0080	±	0.0000	0.0066	±	0.0001	0.0029	±	0.0001
O	0.0010	±	0.0000	0.0103	±	0.0019	0.0060	±	0.0011
P	0.0009	±	0.0000	0.0029	±	0.0001	0.0034	±	0.0001
S	0.0016	±	0.0001	0.0017	±	0.0003	0.0019	±	0.0003
Si	0.0230	±	0.0000	0.0322	±	0.0015	0.0316	±	0.0015
Ta	0.1167	±	0.0058	0.0991	±	–	0.1120	±	–
Ti	0.0010	±	0.0000	<0.0008	±	–	<0.0008	±	–
V	0.2000	±	0.0000	0.1890	±	0.0040	0.1900	±	0.0040
W	1.1033	±	0.0058	1.2000	±	0.0300	1.1700	±	0.0300

Results

Thermodynamic simulation

Given the chemical analysis provided in Table 1 thermodynamic simulations were carried out using ThermoCalc to determine phase fraction and phase compositions. The overall amount of material was 1 mol for the simulations. Fig. 1 presents the mole fraction of the thermodynamic stable phases in dependence on the temperature for all three EUROFER compositions. Since the materials have seen 760 °C or 780 °C in the last step of the heat treatment, austenite cannot be observed; all materials are ferritic-martensitic. MnS, Z-phase and TaN were not observed during our actual investigation. The simulations show that for all materials the TaC phase precipitates between 1100 °C and 1200 °C. Since all samples have seen maximum 980 °C during the austenitization step, it can be assumed that TaC remains unchanged during the heat treatment. For the VN phase a similar argumentation holds, since the austenitization temperature does not exceed the dissolution temperature of VN, which is lowest for EF3s with roughly 1040 °C. The third observed phase i.e., $M_{23}C_6$ precipitates during the tempering step at 760 °C–780 °C. Table 2 summarizes the composition of the most important phases i.e., Fe-Cr martensitic matrix, the $M_{23}C_6$ and TaC-type carbides, as well as the VN for three EUROFER materials. For the Fe-Cr matrix an iron content of about 90 at% and a Cr content of about 9 at% is predicted for all materials. The W content in the matrix is 0.3 at% at maximum. All other elemental contents are below that concentration and considered as trace element. For the $M_{23}C_6$-type carbides the elemental composition ratio Cr:Fe:C is about 2:1:1, respectively. W is accumulated here with about 4–4.5 at% and the Mn content is slightly elevated compared to the Fe-Cr matrix. In case of VN the V:N ratio is

roughly 1:1, with a few at% of Ta and C. For TaC elemental contents are reversed compared to VN as can be seen in Table 2. The calculated compositions will be compared with measured STEM-EDX quantification data further down.

Chemical analysis

Fig. 2 shows the results of a combined SEM-EBSD-EDX measurement in sample EF3i. Fig. 2a shows an inverse pole figure (IPF) underlaid by an image quality map. Dark lines denote grain boundaries or dislocations, whereas dark "dots" correspond to non-indexed precipitate phases. In addition, the IPF proves the martensitic nature of the material.

Comparing the IPF to the Cr map shown in Fig. 2b it is evident that the $M_{23}C_6$ phase is preferentially located at boundaries such as lath or package boundaries. Furthermore, the V map show single, lager sized VN precipitates (some marked by the red arrows in Fig. 2c). The Fe map in Fig. 2d is contrary to the V and Cr map.

From a lower magnified map, which is not shown here the prior austenite grains (PAG) were reconstructed according to method described by Niessen et al. [28]. The resulting PAG grain sizes as well as the martensitic lath widths are listed in Table 3. However, SEM-EBSD has a spatial resolution limit [29], which is in the order of magnitude of the lath widths. Furthermore, orientational issues such as for example as described in Fig. 2 of [29]. The reconstructed PAG grain sizes lie in between 4.5 μm and about 6.5 μm depending on the sample and the reconstruction relationship being used. The martensitic lath size was determined by two methods: (i) extracted from EBSD data and (ii) measured by hand in TEM images. Both methods have advantages and disadvantages. The EBSD values are smaller compared to the TEM values. However, it has to be noted that in the EBSD analysis more values
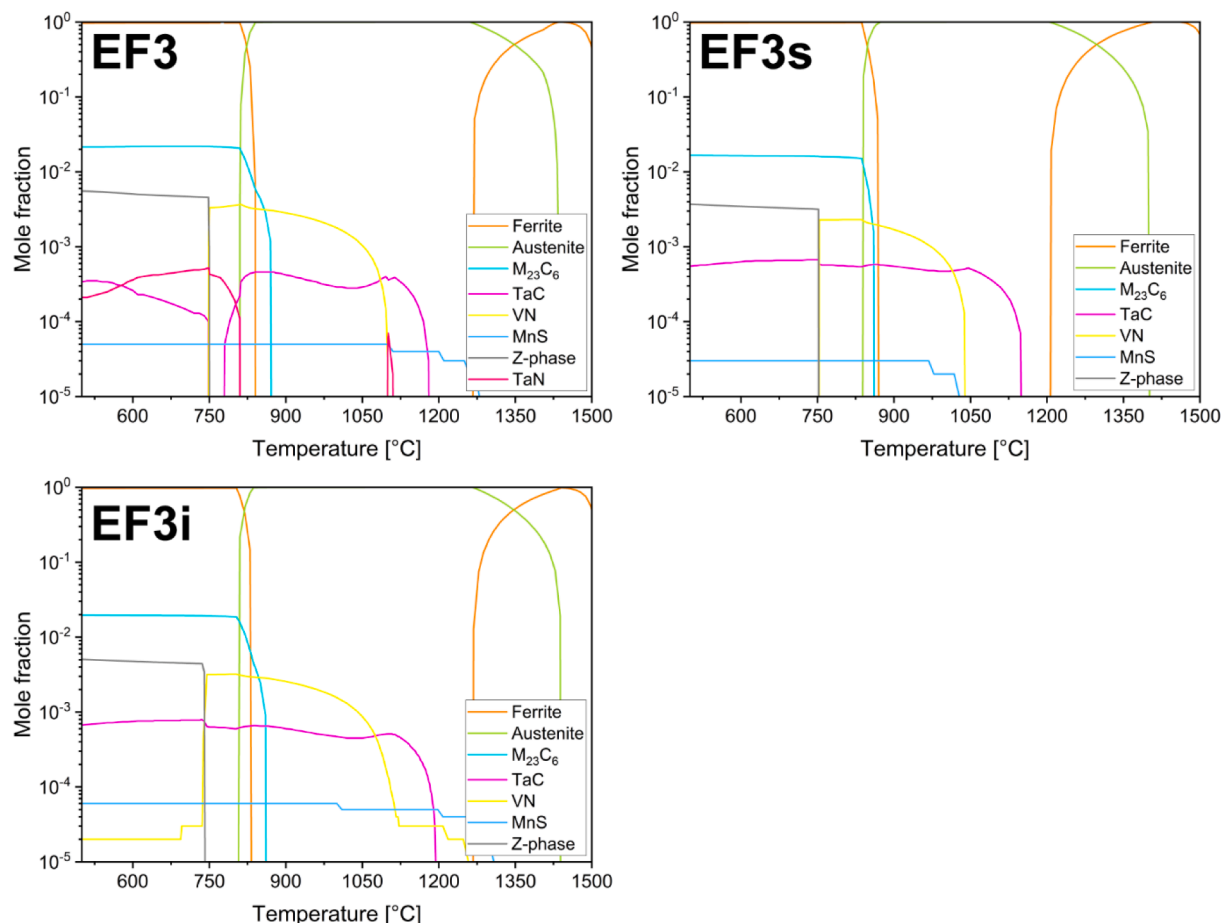

Fig. 1. ThermoCalc simulation of the mole fraction of selected phases in dependence on the temperature for all three EUROFER materials.

Table 2

ThermoCalc calculation of the composition of the single phases observed by TEM.

| Material	Element	Ferrite	$M_{23}C_6$	VN	TaC
		Composition [at%]	Composition [at%]	Composition [at%]	Composition [at%]
EF3i	C	0.0	20.7	2.7	46.9
	N	0.0	0.0	45.2	3.1
	V	0.1	1.0	47.3	1.5
	Cr	8.7	49.9	1.6	3.2
	Mn	0.5	0.9	0	0.0
	Fe	90.4	23.0	0.2	0.0
	Ta	0.0	0.0	2.3	44.8
	W	0.3	4.5	0.0	0.0
EF3	C	0.0	20.7	2.5	45.5
	N	0.0	0.0	45.8	4.5
	V	0.0	0.7	45.6	1.3
	Cr	9.0	49.5	2.6	3.6
	Mn	0.4	0.6	0.0	0.0
	Fe	90.2	24.1	0.2	0.0
	Ta	0.0	0.0	3.4	45.1
	W	0.2	4.3	0.0	0.0
EF3s	C	0.0	20.7	3.3	47.4
	N	0.0	0.0	44.3	2.6
	V	0.1	1.4	48.6	1.9
	Cr	9.3	49.9	1.4	3.1
	Mn	0.0	0.0	0.0	0.0
	Fe	90.2	23.2	0.2	0.0
	Ta	0.0	0.0	2.1	45.0
	W	0.3	4.4	0.0	0.0
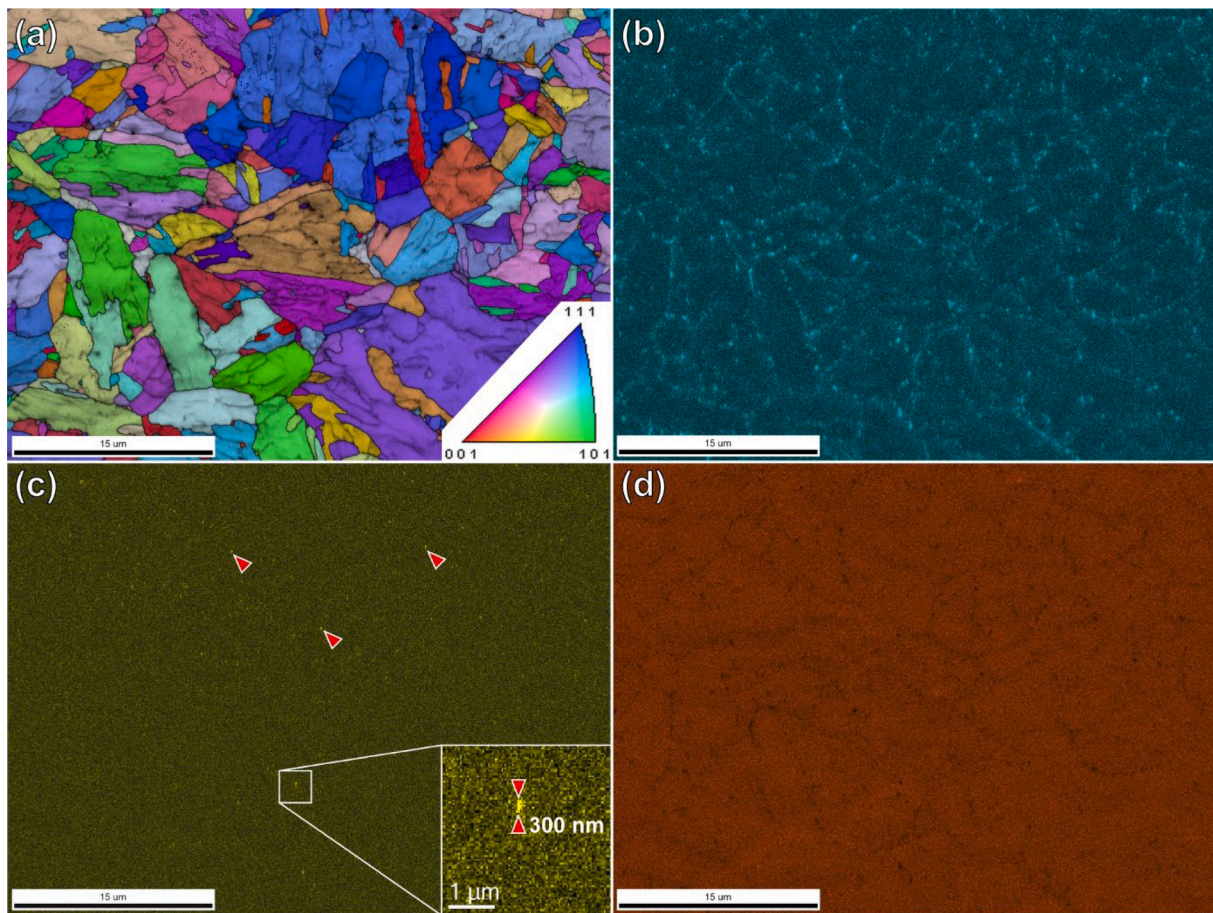
Fig. 2. Results of a combined SEM-EBSD-EDX analysis of sample EF3i. (a) Inverse pole figure. (b)-(d) Cr, V, and Fe elemental map. The scalebar is 15 µm. The inset shows a magnified view of a 300 nm sized VN precipitate.

Table 3

PAG grain sizes and martensitic lath width for the analyzed samples. The values were determined by fitting a log-normal distribution to the grain size histogram and extracting the average grain size. The provided errors are due to the fitting process. K-S denotes the Kurdjumov-Sachs and N-W Nishiyama-Wassermann orientation relationship between martensite and austenite.

Sample	PAG grain size (K-S) [μm]	PAG grain size (N-W) [μm]	Martensitic lath width (EBSD) [μm]	Martensitic lath width (TEM) [μm]
EF3	4.48 ± 0.41	6.61 ± 1.22	0.37 ± 0.03	0.75 ± 0.16
EF3s	4.94 ± 0.49	5.84 ± 0.58	0.26 ± 0.09	0.82 ± 0.32
EF3i	5.89 ± 0.22	6.56 ± 0.30	0.37 ± 0.01	0.61 ± 0.22

(several 100) were used than in the TEM analysis, where only a handful measurements were done by hand. Nonetheless, both methods provide an experimentally based value range for the martensitic lath size that can be used to estimate the material strength.

The TEM characterization of precipitates is carried out at two different magnifications for all three samples using EDX elemental mapping. The results are summarized in Fig. 3 and Fig. 4, respectively. Fig. 3 images roughly an area of 9 μm by 9 μm and contains three types of images: HAADF Z-contrast images, STEM diffraction contrast images (DF4) and a composite image overlaying the Cr, V, and Ta elemental map to image the occurring precipitates in EUROFER. It provides a spatial overview on the material microstructure and chemistry that links TEM results to SEM data in Fig. 2. For all three samples i.e., EF3i, EF3 and EF3s the $M_{23}C_6$-type precipitates are identified by their main element Cr. The $M_{23}C_6$ precipitates are preferentially located at prior austenite grain (PAG), package and lath boundaries. This becomes evident if the Cr map (cyan color) is compared the STEM diffraction contrast images (DF4). Besides the $M_{23}C_6$-type precipitates also MX-type precipitates are present in all analyzed materials although it is hard to recognize them at this magnification. However, in sample EF3i a few larger (120–180 nm in size) MX particles are observed, and one can see that they split into two types, TaC and VN. Other types of precipitates like for example MnS that were observed in earlier modification of
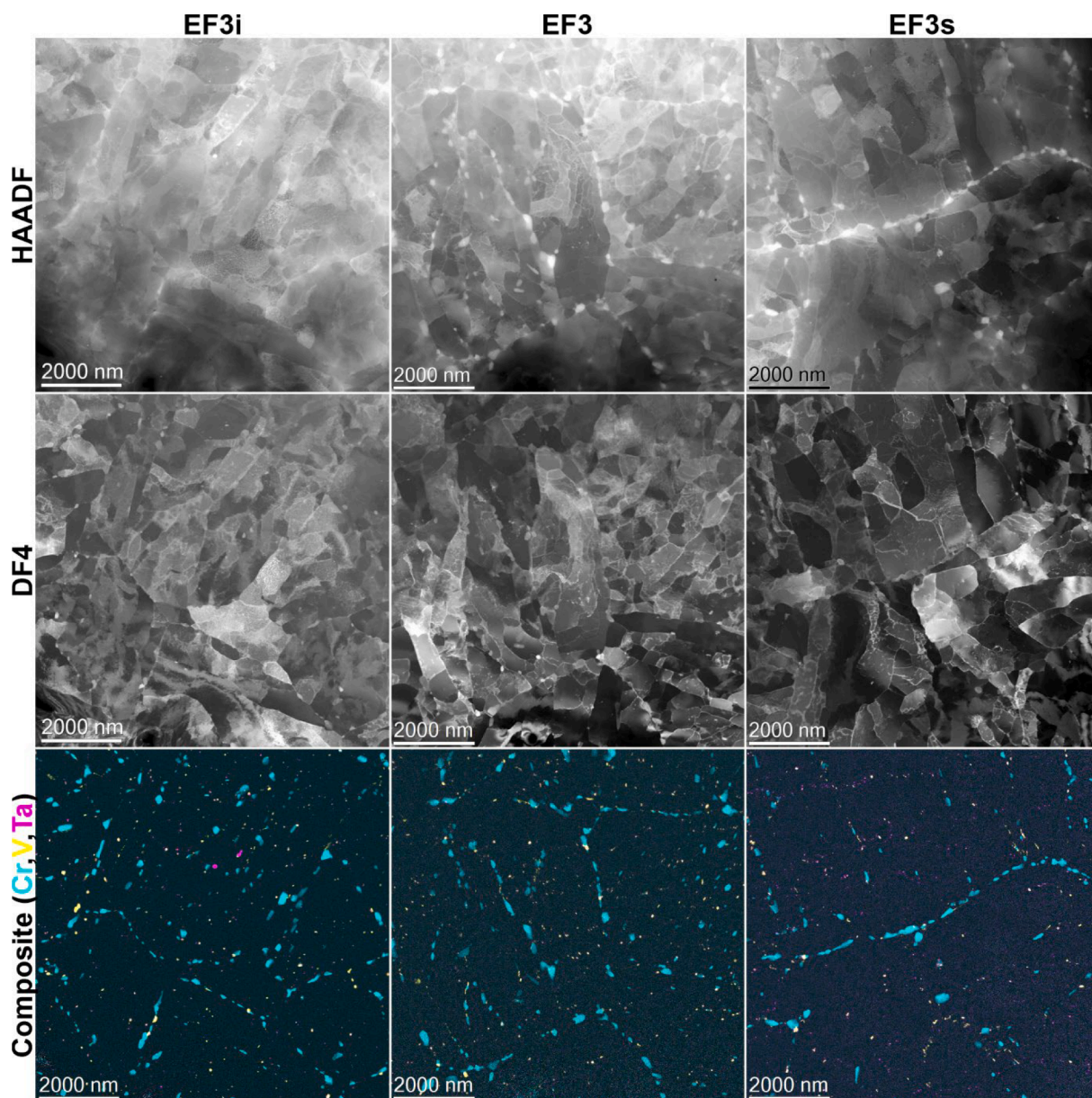

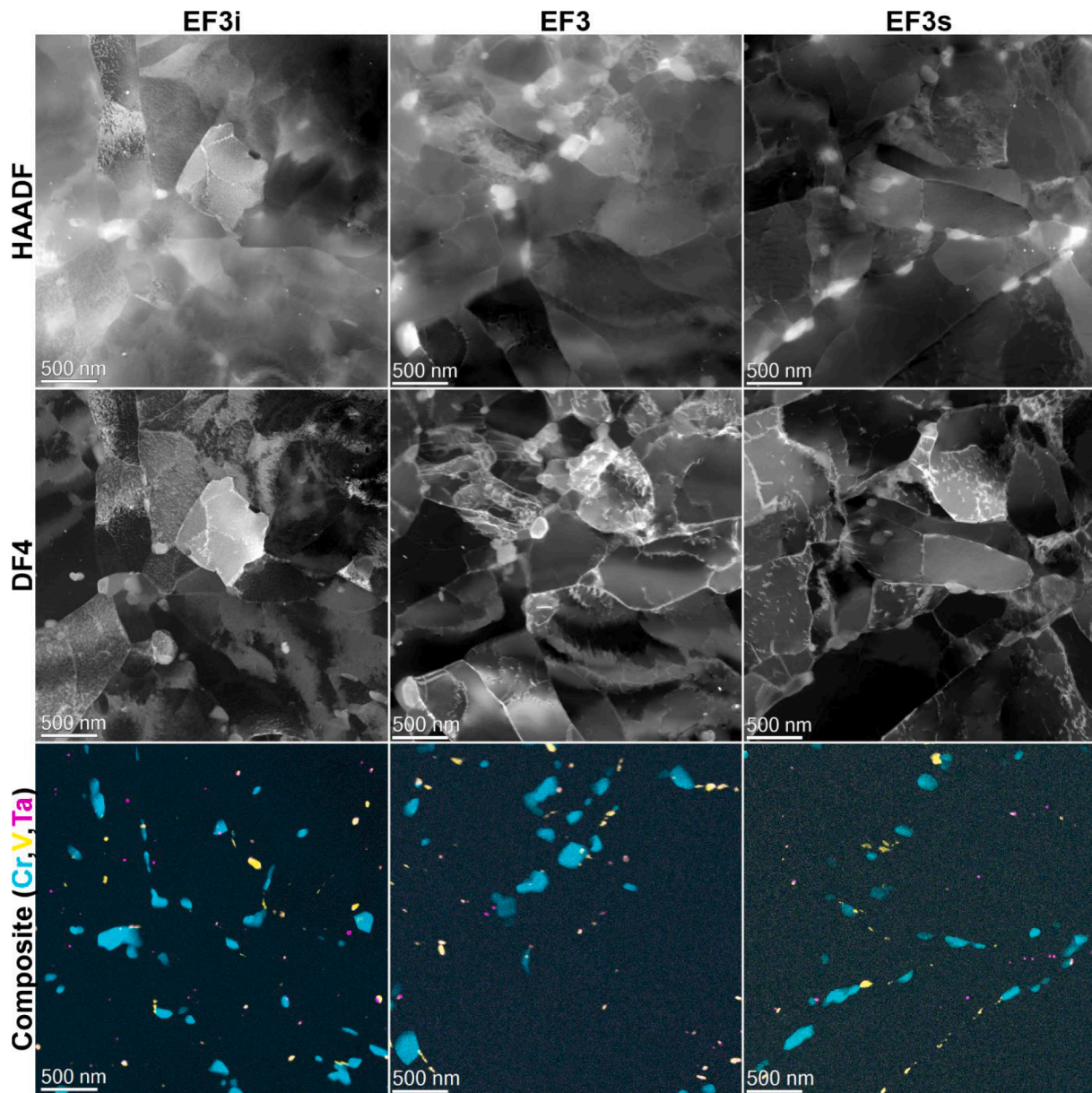**Fig. 3.** Comparative STEM-EDX analysis of all three materials at lower magnification (8.8 μm × 8.8 μm).

Fig. 4. Comparative STEM-EDX analysis of all three materials at higher magnification (3.1 μm × 3.1 μm).

EUROFER are rare (5 in all acquired STEM-EDX maps).

In order to study the MX-type precipitates in more detail higher magnified maps were acquired as can be seen in Fig. 4. By studying the single elemental maps (Cr, V, and Ta) in Fig. 4 it is immediately evident that the MX phases split into larger VN and smaller TaC. A general trend in all analyzed samples seems to be that $M_{23}C_6$ and MX-type particles are often in close vicinity. For VN this is more likely than for TaC, which are randomly distributed. A possible explanation can be obtained by looking at Fig. 1, where one can see that TaC is first type of precipitate nucleating around 1150–1200 °C followed by VN at 1050–1100 °C. Thus, both are mainly nucleating or modified during austenitization. The $M_{23}C_6$ is the last type of analyzed precipitates to nucleate. Nucleation upper limit is about 850 °C with grain boundaries and close by MX-type particles acting as nucleation centers for $M_{23}C_6$.

For each material 4 (2 at lower and 2 at higher magnification) STEM-EDX maps were evaluated quantitatively regarding particle size distribution, particle shape, and particle number density. The sample thickness needed for determining the precipitate number density was extracted from low loos EELS datasets. The results involving several

hundred precipitates in each material are summarized in Fig. 5 and.

Table 4. The precipitates' grain sizes measured from STEM-EDX elemental maps by determining Feret's diameter. The grain sizes follow in all cases a log-normal size distribution. Fig. 5a and b present the grain size and circularity evaluation of the $M_{23}C_6$-type precipitates for all three EUROFER materials. On average the $M_{23}C_6$ precipitates in EF3 are with 137 nm the smallest, whereas they are in sample EF3s with an average size of 152 nm the largest. Outlier $M_{23}C_6$ grains have sizes of up to about 700 nm. The circularity value, which is a measure for the roundness of the particles, resides for the $M_{23}C_6$ precipitates roughly between a value of 0.7 and 0.8 in all analyzed EUROFER materials indicating elongated particles as can be seen in Fig. 5b. The MX-type precipitates i.e., TaC and VN, are by a factor 3–5 smaller on average than the $M_{23}C_6$ precipitates for all three analyzed materials as can be seen in Fig. 5c and e. Furthermore, the circularity values for both MX-type phases lie above a value of 0.9 for all analyzed materials indicating an almost circular shape of the precipitates.

The particle number densities lie for all materials and all types of precipitates in range of 10^{19} particles per cubic meter. The errors are due
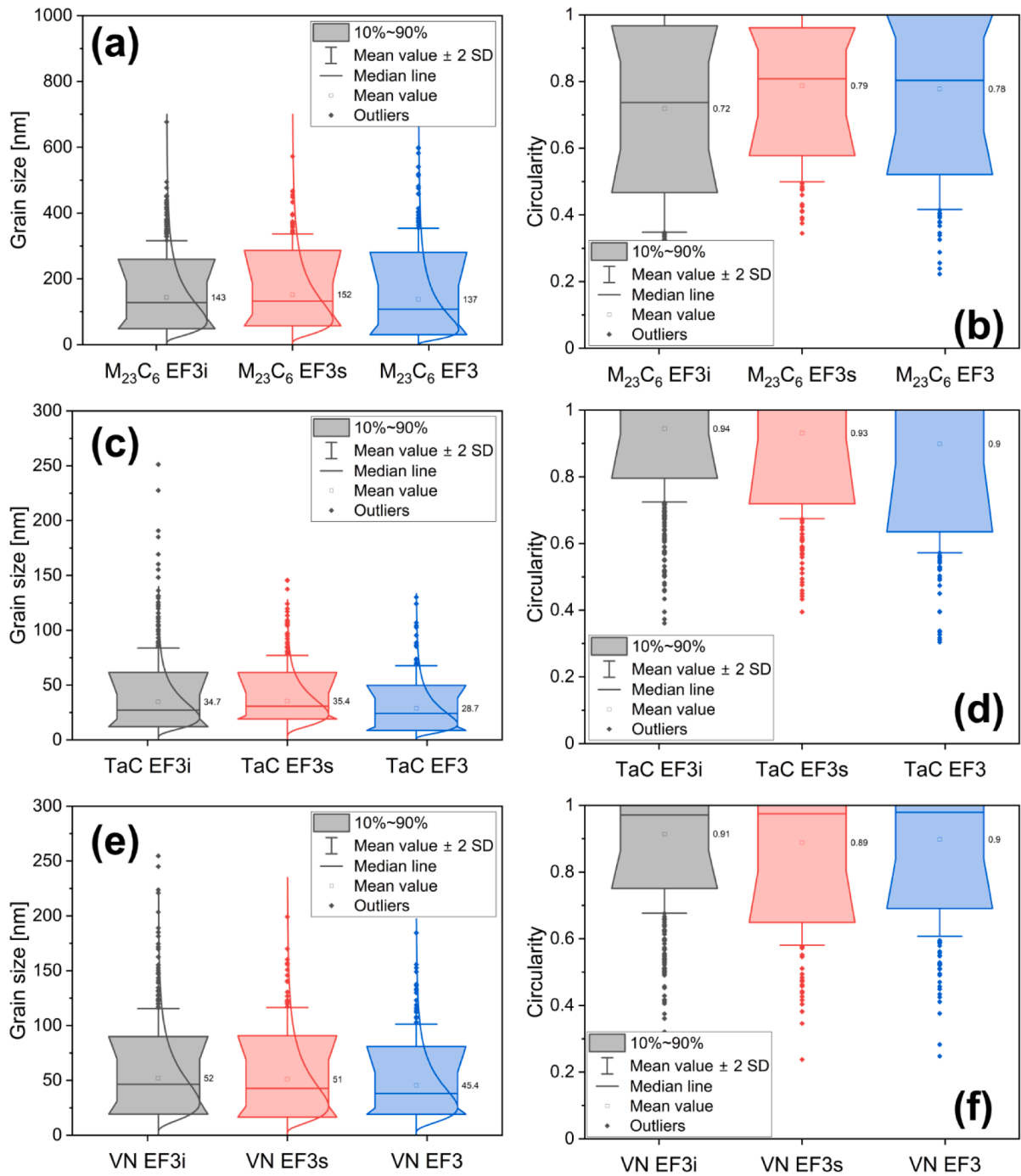
Fig. 5. (a), (c), (e) Statistical grain size graphs for the $M_{23}C_6$, TaC, and VN phase in all materials, respectively. (b), (d), (f) contains the circularity value for the $M_{23}C_6$, TaC, and VN phase in all materials, respectively.

Table 4
Particle number densities and average NND for $M_{23}C_6$ and MX-type phases.

Phase	Sample	Number density [m^{-3}]			Average NND [nm]		
$M_{23}C_6$	EF3i	$3.21\ 10^{19}$	$\pm$	$6.61\ 10^{18}$	274.6	$\pm$	155.4
	EF3	$4.45\ 10^{19}$	$\pm$	$9.65\ 10^{18}$	308.8	$\pm$	191.5
	EF3s	$3.31\ 10^{19}$	$\pm$	$7.29\ 10^{18}$	310.1	$\pm$	207.5
TaC	EF3i	$8.17\ 10^{19}$	$\pm$	$1.68\ 10^{19}$	137.5	$\pm$	103.1
	EF3	$6.79\ 10^{19}$	$\pm$	$1.51\ 10^{19}$	175.5	$\pm$	161.8
	EF3s	$4.94\ 10^{19}$	$\pm$	$1.09\ 10^{19}$	123.5	$\pm$	107.2
VN	EF3i	$6.34\ 10^{19}$	$\pm$	$1.31\ 10^{19}$	156.0	$\pm$	120.2
	EF3	$6.00\ 10^{19}$	$\pm$	$1.32\ 10^{19}$	158.0	$\pm$	124.0
	EF3s	$4.34\ 10^{19}$	$\pm$	$9.59\ 10^{18}$	170.9	$\pm$	181.4

to measurement and data evaluation inaccuracies like for example sample thickness determination or particle separation errors. In case of $M_{23}C_6$ the number densities are more less comparable for all three materials. For TaC the precipitate number densities decrease from $(8.17 \pm 1.68)\ 10^{19}$ precipitates per m^{-3} found in EF3i to $(4.94 \pm 1.09)\ 10^{19}$ precipitates per m^{-3} in EF3s. For the VN a similar trend is observed, though, the number density values are slightly smaller than for TaC. In case of the average nearest neighbor distance (NND), the values increase from 275 nm (sample EF3i) to 310 nm (sample EF3s) for the $M_{23}C_6$-type precipitates. For both MX-type precipitates i.e., TaC and VN the NND ranges from about 124 nm to about 176 nm, which is significantly less than for the $M_{23}C_6$ phase. For all phases the error values exceed 100 nm,

which is quite large compared to the average NND values and indicates large datapoint scatter.

A statement on the mean composition as well as on the spatial phase distribution can be obtained by decomposing STEM-EDX datasets via principal component analysis (PCA) [30]. In detail a non-negative matrix factorization (NMF) algorithm was used for decomposition to aid the physical interpretation of components from spectral datasets such as for example EDX or EELS [31]. Fig. 6 contains the results of such a NMF analysis, where the principal components are sorted according to their proportion of variance (see also left lower graph in Fig. 6). The point at which the graph becomes linear indicated by the dashed line separates the significant components on the left-hand side from the noise on the right-hand side. The results of the NMF split in two parts the "loadings" which contain in our case the spatial distribution of the components and the "factors" which contain spectral component data. The loadings i.e.,

phase maps are presented in the upper two image rows in Fig. 6 along with the corresponding HAADF image and a composite image overlaying the single precipitate maps. Fig. 6 confirm the finding that the MX-type precipitates split into two species, namely VN and TaC. The components' factors have the form of EDX spectra and are summarized in the lower right graph. From this graph it is evident that besides the matrix three types of precipitates are present namely $M_{23}C_6$, VN, and TaC. Other precipitates might be present but are too few to be recognized using NMF and their contribution is thus hidden in the noise. These factors can be quantified using standard EDX quantification methods.

Table 5 presents the results of a quantification of the NMF extracted STEM-EDX data of all three EUROFER materials. In case of the Fe-Cr matrix the Fe content is overestimated, whereas the Cr content is underestimated for all three materials compared to the predicted
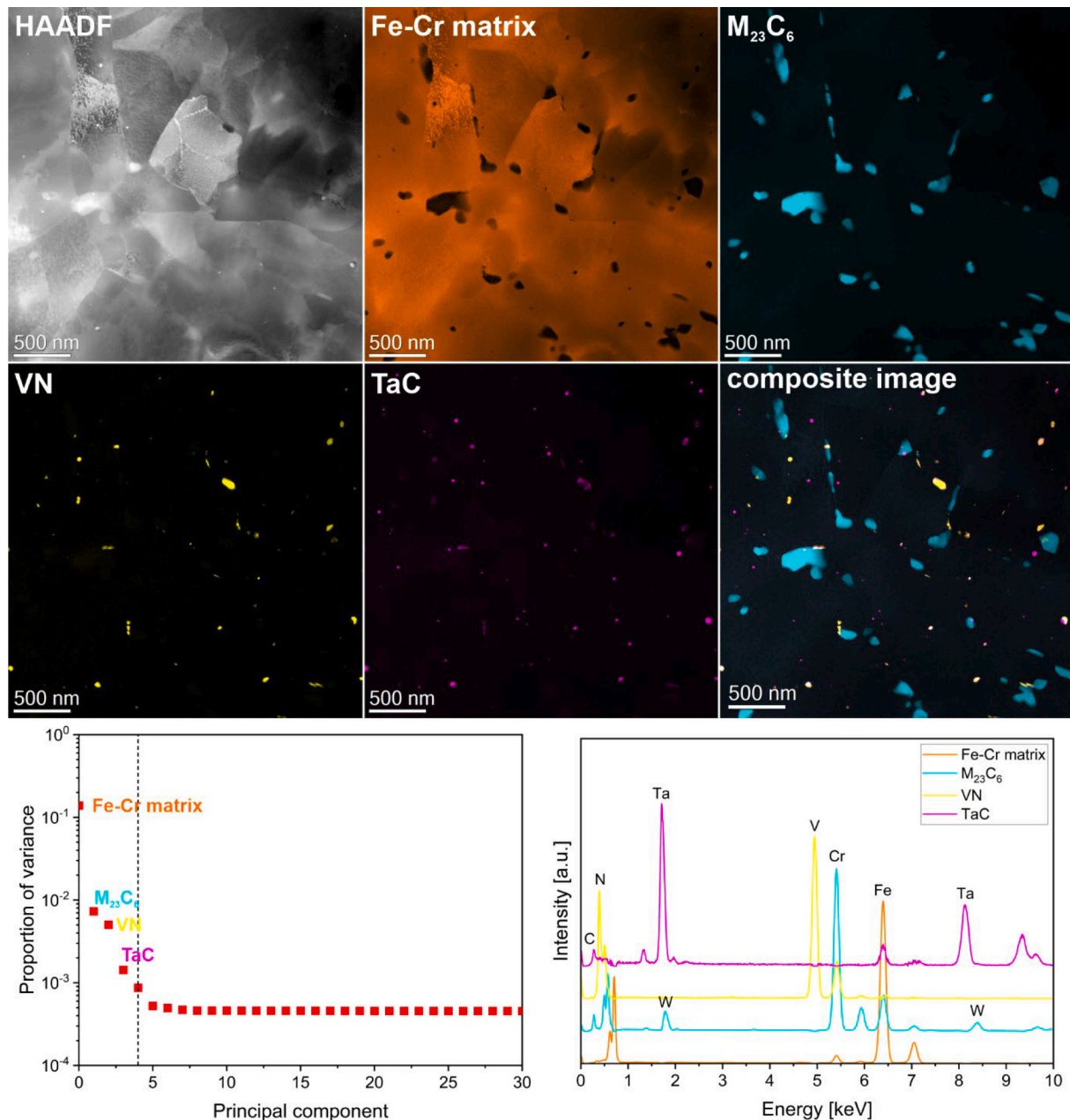

Fig. 6. Principal component analysis (PCA) of a STEM-EDX dataset acquired in sample EF3i using the NMF algorithm. The first four principal components with the largest variance correspond to the four main phases i.e., the Fe-Cr matrix, $M_{23}C_6$, VN and TaC, respectively. The presented maps are the NMF "loadings", and the spectra are the "factors" that were calculated by Hyperspy.

Table 5

Quantification of STEM-EDX data analyzed by NMF.

Phase	Element	Shell	k-Factor (/Si)	Composition EF3i at.%			Composition EF3 at.%			Composition EF3s at%		
Fe-Cr matrix	C	K	1.647	0.1	±	0.1	1.7	±	0.2	0.0	±	0.0
	N	K	1.305	1.9	±	0.2	1.1	±	0.2	0.1	±	0.1
	V	K	1.225	0.0	±	0.0	0.0	±	0.0	0.0	±	0.0
	Cr	K	1.240	4.0	±	0.2	5.0	±	0.2	4.9	±	0.2
	Mn	K	1.307	0.6	±	0.1	0.5	±	0.1	0.2	±	0.1
	Fe	K	1.333	93.3	±	0.2	91.6	±	0.2	94.8	±	0.2
	Ta	L	2.021	0.0	±	0.0	0.0	±	0.0	0.0	±	0.0
	W	L	2.058	0.0	±	0.0	0.0	±	0.0	0.0	±	0.0
$M_{23}C_6$	C	K	1.647	19.2	±	1.2	21.9	±	1.3	16.8	±	1.1
	N	K	1.305	0.6	±	0.2	0.6	±	0.3	0.5	±	0.3
	V	K	1.225	0.0	±	0.0	0.0	±	0.0	0.0	±	0.0
	Cr	K	1.240	60.3	±	0.8	61.5	±	0.8	62.4	±	0.8
	Mn	K	1.307	2.2	±	0.4	1.8	±	0.4	1.1	±	0.4
	Fe	K	1.333	14.8	±	0.6	11.5	±	0.5	16.5	±	0.6
	Ta	L	2.021	0.0	±	0.0	0.0	±	0.0	0.0	±	0.0
	W	L	2.076	3.0	±	0.2	2.7	±	0.2	2.7	±	0.2
VN	C	K	1.647	0.0	±	0.0	0.0	±	0.0	0.9	±	1.1
	N	K	1.305	52.0	±	3.0	52.0	±	3.0	47.0	±	3.0
	V	K	1.223	43.1	±	1.2	38.8	±	1.4	37.1	±	1.3
	Cr	K	1.240	4.8	±	0.9	7.4	±	0.9	4.7	±	0.9
	Mn	K	1.307	0.1	±	0.4	0.1	±	0.4	0.0	±	0.4
	Fe	K	1.333	0.4	±	0.4	1.1	±	0.4	10.4	±	0.8
	Ta	L	2.021	0.0	±	0.0	0.6	±	0.3	0.0	±	0.0
	W	L	2.076	0.0	±	0.0	0.0	±	0.0	0.0	±	0.0
TaC	C	K	1.647	38.0	±	5.0	44.0	±	4.0	35.0	±	5.0
	N	K	1.305	3.0	±	2.0	19.0	±	2.0	5.0	±	3.0
	V	K	1.225	0.0	±	0.0	0.0	±	0.0	0.0	±	0.0
	Cr	K	1.240	0.0	±	0.0	0.0	±	0.0	0.0	±	0.0
	Mn	K	1.307	0.0	±	0.0	0.2	±	0.5	0.0	±	0.0
	Fe	K	1.333	13.7	±	1.9	13.0	±	1.2	3.7	±	1.2
	Ta	L	2.021	45.7	±	1.1	23.7	±	0.6	55.7	±	1.1
	W	L	2.076	0.1	±	0.9	0.1	±	0.4	0.2	±	1.0

composition summarized in.

Table 2. The Mn content is measured correctly within the error margins. In case of C and N contents the thermodynamic calculation summarized in Table 2 predicts zero content for both elements in the Fe-Cr matrix. However, there is always some C and N for example on the surface or the spectral background is not reproduced correctly by the NMF decomposition leading to non-zero elemental contents as can be seen for sample EF3 in Table 5. Also, a non-perfect decomposition might explain the non-zero C and N contents in the Fe-Cr matrix.

The extracted $M_{23}C_6$ compositions in Table 5 are similar to each other i.e., the compositions are within the provided error ranges. However, compared to the predictions summarized in Table 2 it becomes evident that in the experiment the Cr content is overestimated by about 10 at% and at the same time the Fe content is underestimated by the same amount. In addition, the W content of the $M_{23}C_6$ phase is about 1–2 at% lower in the experiment as in the ThermoCalc prediction. The carbon content, however, is well reproduced except for sample EF3s, where it is underestimated by about 4 at% due to the already above-mentioned reasons.

Both the VN and TaC phase are similar with respect to their main element contents i.e., V, N and Ta, C, respectively. The experimental content values can differ especially for the light elements C and N but also for other elements due to imperfect decomposition and spectral fits. Furthermore, ThermoCalc predicts a Fe composition of max. 0.2 at% for both phases, which is in some cases exceeded by about 10 at%.

Finally, higher magnified combined STEM-EDX-EELS measurements were acquired of a PAG part as can be seen in Fig. 7. Both STEM-EDX and STEM-EELS maps show a Cr enrichment at the PAG (see red triangle in the Cr maps). However, Cr is not the only element being enriched at the PAG. STEM-EDX provides evidence that also Mn and W accumulates at the PAG. In addition, C enrichment at boundaries is observed via STEM-EELS. All four elements i.e., C, Cr, Mn, and W are associated with the $M_{23}C_6$ phase.

Structural analysis

Fig. 8a shows a TEM bright-field image of a martensite lath (4 μm long dark region close to the image center), which is oriented in a [1 1 0] zone-axis orientation. The dashed circle denotes the position of the selected area aperture, which was used to acquire the diffraction pattern presented in Fig. 8b. In the diffraction pattern two kinds of spots. The strong, red encircled spots belong to the martensite matrix, which oriented in a [1 1 0] zone-axis. For simplicity reasons the crystal structure of ferrite (ICSD No. 52258) was used to fit the diffraction pattern. This simplification is justified since the tetragonal distortion of the martensite differs for our material about 1% from the ferrite, which about the resolution that can be achieved using a CCD-based detection system in a TEM. The martensite lattice constants were calculated according to Roberts [32] using the carbon contents given in Table 1 and the ferrite lattice constant. A close match for the weaker spots marked by the yellow triangles could be Cr_3C_2 oriented in a [1 0 0] zone-axis orientation, possibly present in form of a thin surface layer.

Close to the oriented martensite grain a $M_{23}C_6$ grain was found whose orientation was close to [1 1 0] zone-axis orientation. In EUROFER-type steels the main metal component of these carbides is chromium. It is shown in the TEM bright-field image in Fig. 8c. The dashed white circle denotes the size and position of the selected area aperture needed to acquire the diffraction pattern presented in Fig. 8d. The red encircled spots belong to the $M_{23}C_6$ structure (ICSD No. 62667). The stronger reflections in between are due to the surrounding martensite matrix. The same grain was also imaged via high-resolution phase contrast imaging. The result is presented in Fig. 8e. The inset reveals that a dislocation is intersecting the precipitate. Fig. 8f is the corresponding Fast-Fourier Transformation (FFT), which coincides well with the precipitates' diffraction pattern shown in Fig. 8d. The inset Fig. 8f is the FFT of the inset in Fig. 8e and exhibits streaking along the ⟨1 1 1⟩ direction, which is due to the dislocation lying in one of these
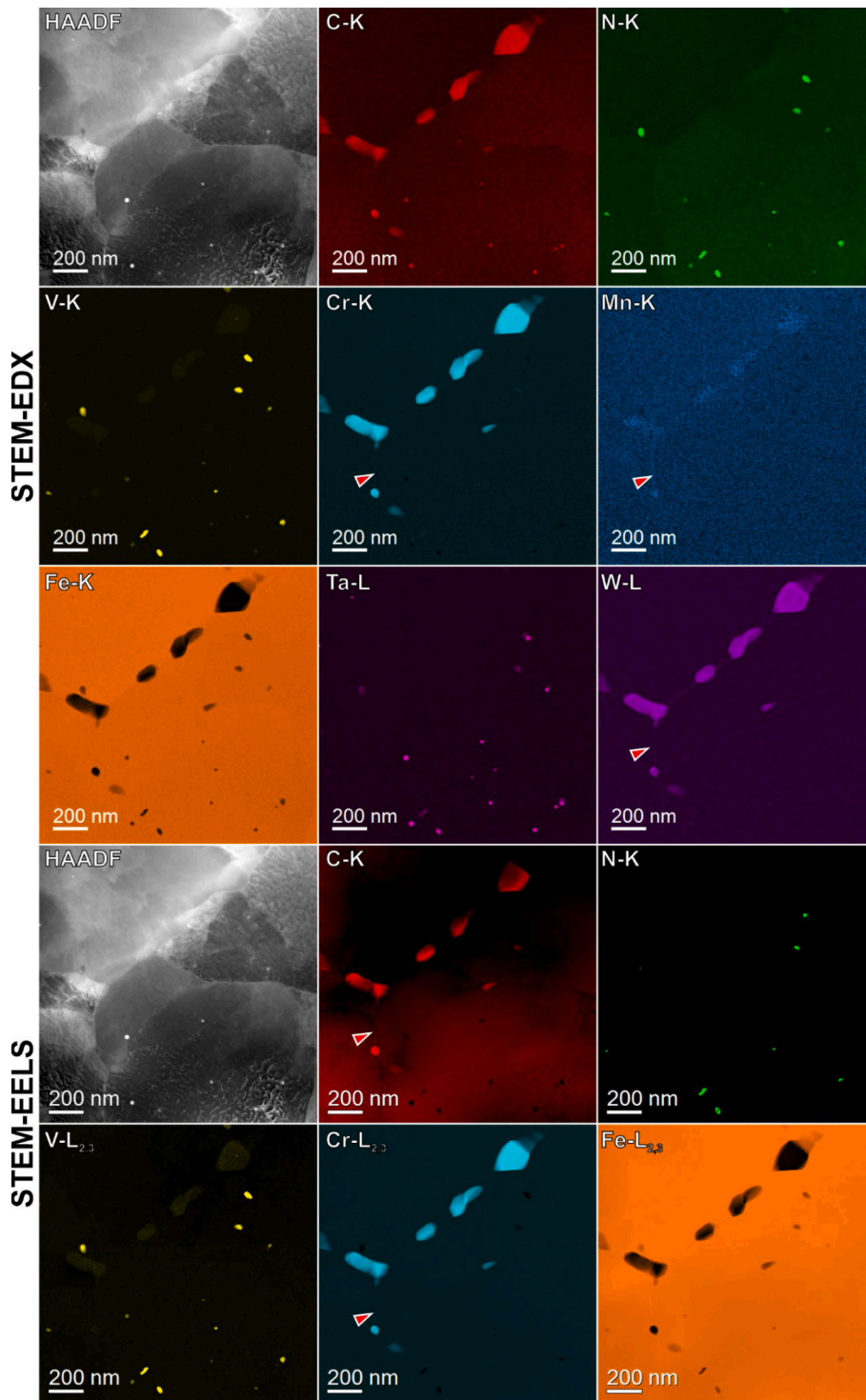
Fig. 7. Combined STEM-EDX/-EELS measurement documenting that elements forming the $M_{23}C_6$ phase are mobile along martensitic grain boundaries at elevated temperatures.

planes.

The presence of Cr_3C_2 is a common issue, since a second grain that can be seen in the bright-field image in Fig. 9. The part in the white rectangle contains an interesting region is magnified. The result is shown in Fig. 9b and c in form of high-resolution phase contrast images. The martensite grain has a [1 1 0] zone-axis orientation as can be seen by the red encircled spots in the FFT presented in Fig. 9d. In addition, the line of spots marked by the yellow triangles are present, which are the same as found in Fig. 8 and can be explained by the presence of Cr_3C_2.

The 100 nm sized bean-like grain in Fig. 9b is a $M_{23}C_6$ grain located in a martensite lath boundary. The FFT in Fig. 9e reveals that it is crystalline and oriented along [3 7 0] zone-axis. A VN precipitate is attached to the $M_{23}C_6$ grain as can be seen in Fig. 9c. It has a size of 30 nm and is also crystalline. Fig. 9f is the FFT calculated from the region in the white rectangle in Fig. 9c. It shows that it is oriented in [0 0 1] zone-axis. TaC, which has essentially the same crystal structure as VN can be excluded, since the lattice constant of TaC is about 7% larger than that of VN. Fitting both crystal structures i.e., VN (ICSD No. 22321) and TaC
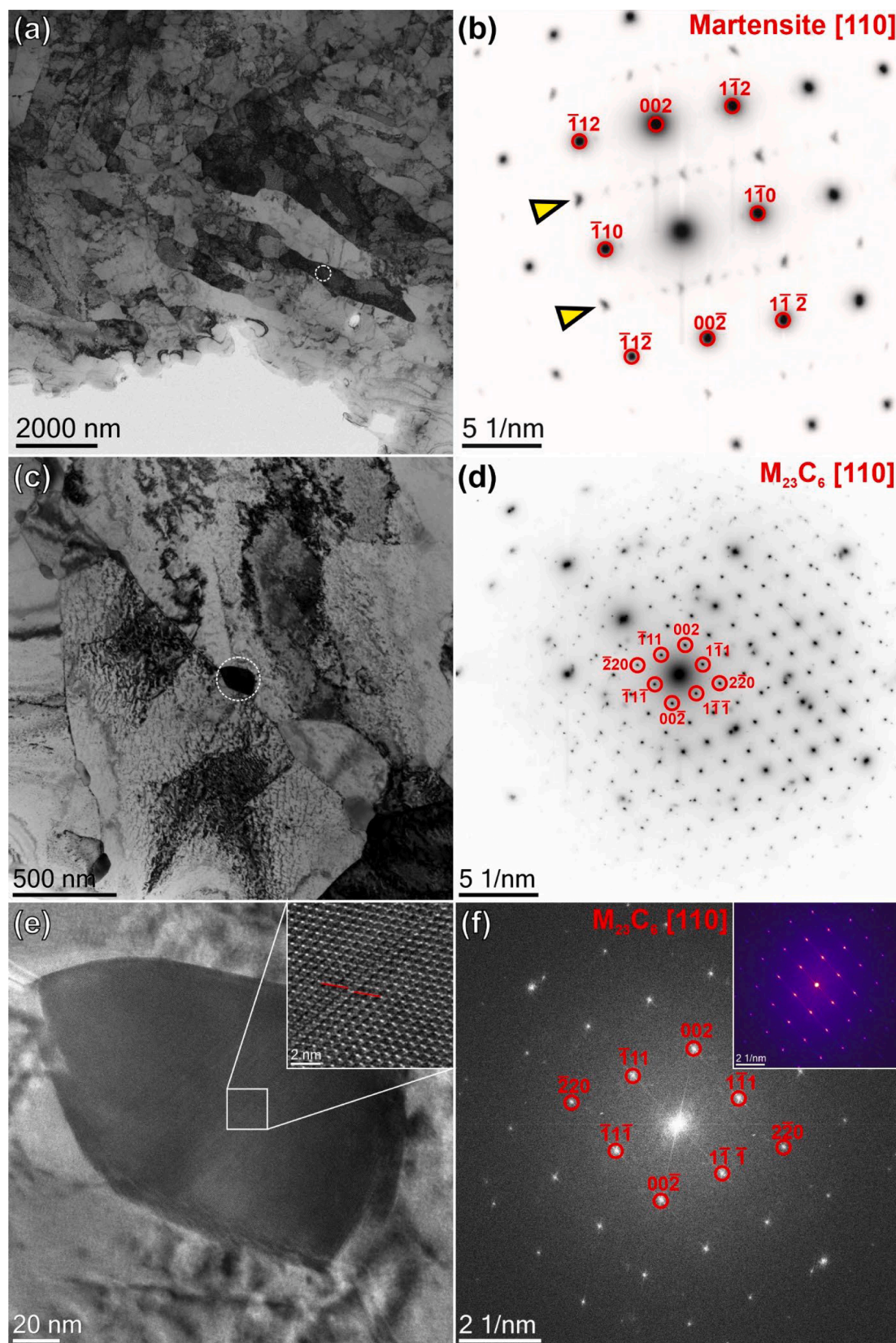
Fig. 8. TEM analysis of sample EF3i. (a) TEM bright-field image and corresponding selected area diffraction pattern of a martensitic lath in [1 1 0] zone-axis orientation. (c) TEM bright-field image of a $M_{23}C_6$ precipitate in [1 1 0] zone-axis orientation with (d) corresponding selected area diffraction pattern. (e) and (f) are a high-resolution phase contrast image and the corresponding Fast Fourier Transformation of the same $M_{23}C_6$ particle shown in (c). The insets show a dislocation crossing the $M_{23}C_6$ particle and the corresponding FFT in false colors.
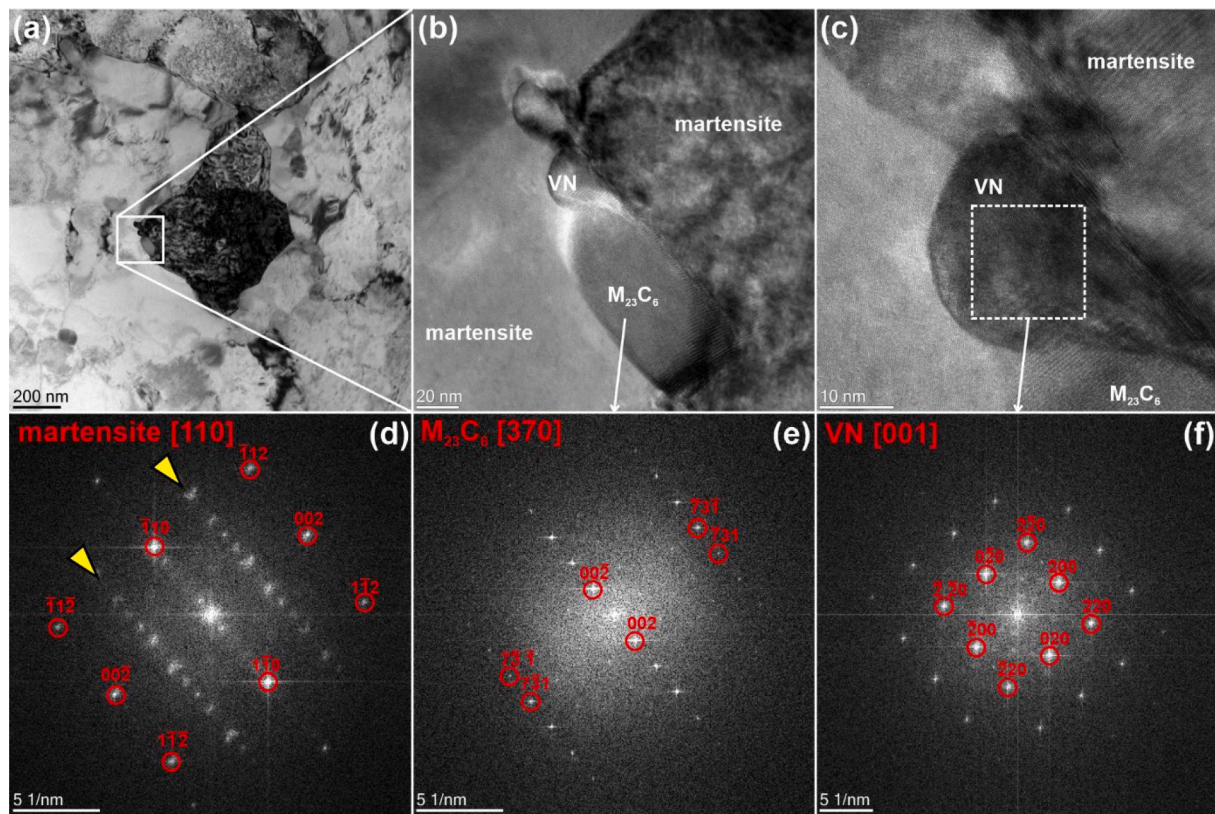
Fig. 9. TEM analysis of sample EF3i. (a) TEM bright-field overview image of the analyzed region. (b) and (c) are high-resolution phase contrast images of a $M_{23}C_6$ and a VN precipitate attached to the dark martensite grain shown in (a), respectively. (d)-(f) Fast Fourier Transformations of the martensite region in (b), the $M_{23}C_6$ grain in (b), and the VN precipitate in (c).

(ICSD No. 159875) to the FFT yields a sum-of-squares error of 3.2 for VN and of 60.2 for TaC, respectively.

Fig. 10 shows high-resolution phase contrast images of isolated particles (agglomerations) in the martensite matrix. Fig. 10a shows a two-particle agglomeration of a VN and a TaC precipitate, which is also known as V-wing. Both precipitates are 15–20 nm in size. The FFT presented in Fig. 10c shows that both precipitates have an orientational relationship to each other. Both are oriented along a common zone-axis, here [3 0 1]. The TaC spots are marked in blue and the VN spots are marked in red. An orientational relationship with the martensite matrix could not be established. Furthermore, isolated single VN precipitates are present in the martensite matrix as can be seen from Fig. 10b. The actual particle is about 70 nm in size and oriented in [0 0 1] zone-axis as it is indicated by the red circles in the FFT in Fig. 10d. Again, no direct orientational relationship with the martensite matrix was found.

Discussion

EUROFER is the European structural candidate material for future fusion power plants. Its development included and included several boundary conditions such as e.g., lifetime at operational conditions at elevated temperatures and neutron irradiation, environmental and economic issues. For an improved efficiency of any power plant a higher operational temperature is required. The current EUROFER material development tries to find an optimum temperature by thermodynamically guided alloying, thermal treatment, and microstructural optimization. In order to understand aging effects occurring for example during creep experiments it is vital to know the structural baseline. In detail, the size and average distance of precipitates as well as their composition. It is known that at elevated temperatures the precipitates in 9Cr steels like e.g. EUROFER are coarsening via an Ostwald ripening, which weakens the pinning of lath and grain boundaries [33].

Thermodynamics

Thermodynamic modelling of RAFM steels began with the material development itself, roughly 30 years ago. Since the material is a multi-element mixture, phase predictions using a CALPHAD approach were continuously developed and improved and still are [34], also in combination with experimental validation [35,36]. Some of the results are now part of the ThermoCalc software libraries [37]. However, the PANDAT software package offers similar possibilities and features [38] and is used in a similar way as ThermoCalc in steel development and qualification [39].

To explain our experimental microstructural findings ThermoCalc simulations regarding the mole fraction of selected phases in dependence on the temperature and the single-phase compositions have been performed.

Comparing our results from Fig. 1 i.e., the phase mole fractions to those of Oliveira et al. [35] it becomes evident that the occurring phases are the same and their temperature range of existence as well as their molar fraction are similar. The Z-phase was included in our calculations; however, it is not relevant for the pristine state of the samples, since the tempering temperature exceeds its limits of existence. It will become important during thermal aging of the samples. The only elements which content is significantly different in one sample compared to the two others and literature data [34,35] is Mn, which was significantly reduced in sample EF3s. Mn will capture sulfur in the steel and form MnS in form of nanoparticles. Reducing the Mn content reduces the amount of MnS particles, which is nicely seen in Fig. 1. Since in the recent steel very little sulfur is present (see Table 1), MnS precipitates are rare and hard to observe in TEM. In addition, the Mn content will mainly influence parameters like the austenite-to-ferrite transition temperature, because Mn is considered as a weak austenite stabilizer or the Ductile-to-brittle transition temperature [40], which will become important during
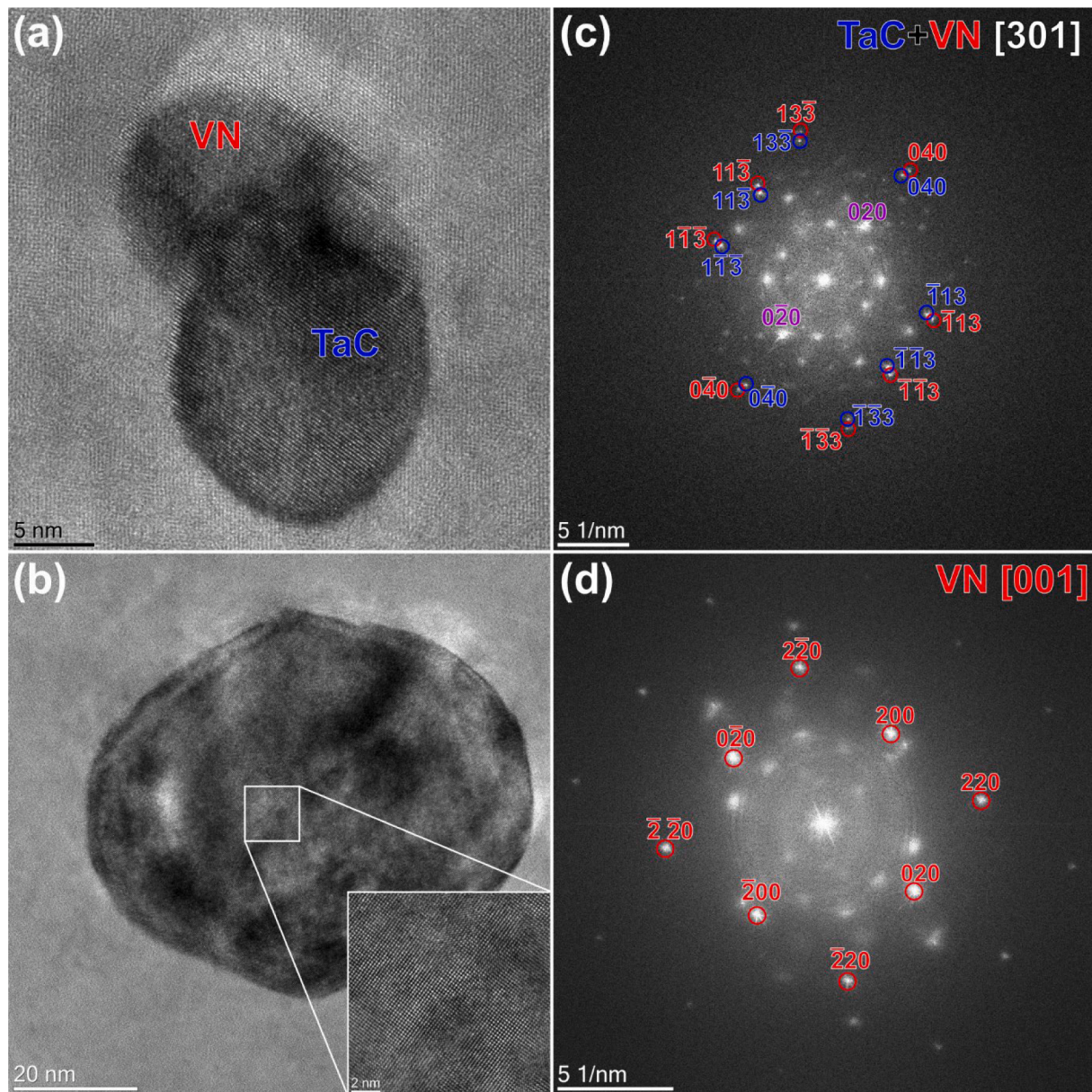
Fig. 10. TEM analysis of sample EF3i. (a) High-resolution phase contrast image of a V-wing and (b) an isolated VN precipitate. The inset shows a magnified view on the crystal structure of the VN precipitate. (c) and (d) are indexed Fast Fourier Transformations of (a) and (b), respectively.

neutron irradiation experiments.

Other elements like V or Ta are considered as ferrite forming elements effective in removing the austenite formers carbon and/or nitrogen from solution as insoluble carbides and nitrides (MX-type precipitates) [40]. This behavior is modeled by ThermoCalc and can be seen in Fig. 1. Our ThermoCalc prediction is in good agreement with that of Oliveira et al. [35] regarding the precipitation sequence of the MX-type phases i.e., first TaC at 1100–1200 °C and then VN at 1050–1100 °C. A similar behavior is also calculated and observed in additively manufactures US 9Cr steels [39]. In our case both temperatures were never reached during the heat treatment i.e., MX-type phases were never in complete solution. Both types of MX precipitates can thus limit in our case the austenite grain growth during the austenitization process due to pinning mechanisms [40]. In addition, it explains why some of the MX particles are located within single laths or grains.

The next phase to precipitate is the $M_{23}C_6$ phase, which is for all our samples around 860 °C. This is what is reported in literature [34,35,39]. That means for our samples the $M_{23}C_6$ are not dissolved during the

tempering step at 760 °C/780 °C. According to Klueh and Harries [40] for temperatures larger than 550 °C $M_{23}C_6$ start to nucleate at martensite lath boundaries and PAGs. If the temperature exceeds 650 °C $M_{23}C_6$ precipitates will grow and virtually all dissolved C will be removed from the matrix and transferred to the $M_{23}C_6$ precipitates if 700 °C or more are applied for more than 1 h. This behavior can also be seen in Table 2, where the predicted phase compositions are listed. The ferrite/martensite phase contains no C. However, on the experimental side, C contamination cannot always be avoided as can be seen above.

The stability of the precipitate phases can be understood by looking at Ellingham diagrams i.e., the Gibbs energy. For the binary transition metal carbides they can be found for example in the work of Shatynski [41]. In the relevant temperature range, which lies in our case in between 500 °C and 1000 °C the Ellingham diagrams show that TaC is the most stable binary transition carbide that can occur in our material. Only V_2C is comparable in stability from an energetically point of view. It is followed VC, Fe_3C. For chromium carbide and manganese carbide the situation is more complicated since several carbides can coexist. In

case of EUROFER for example, both M_7C_3 and $M_{23}C_6$ nucleate at the same time, however, W stabilizes the $M_{23}C_6$ phase and favors the dissolution of the M_7C_3 phase [34].

For the stability of the transition metal nitrides forming the MX-type phases a similar argumentation as for the carbides can be applied. According to Sigler [42] TaN is more stable than VN, however, sub-stoichiometric VN exceeds the standard free energy of formation of TaN. That raises the question why Ta is bound in form of TaC and not TaN in EUROFER-type steels. Danon and Servant [34] found that the overall Ta content determines the fraction between TaC and VN. They also stated that part of the Ta is bound in the VN due to a limited solubility. As mentioned by Oliveira et al. [35] the coexistence of TaC and VN was experimentally observed by several authors in ferritic-martensitic steels, which is also in agreement with our own observations.

The grain boundary microchemistry in aged EUROFER samples was summarized by Fernandez et al. [43]. They experimentally found a Cr enrichment in the EUROFER grain boundaries especially in aged materials. However, as can be seen in Fig. 7 even in pristine material grain boundaries are enriched in certain elements like C, Cr, W and Mn due to the fact that the phase separation process here the formation of the $M_{23}C_6$ precipitate phase is not yet finished during the applied tempering time. The following qualitatively discusses diffusion in bulk material, diffusion along grain boundaries is expected to be stronger especially during the tempering step of the heat treatment. According to Askill [44] the Cr diffusion in an Fe-Cr alloy is strong due to an significant amount of Cr self-diffusion. The Fe diffusion on the other hand is much weaker. It is also found therein by comparing the tracer diffusion values that the diffusion of W in Fe is faster than Fe in W. From first principle calculations of the diffusion of Mn in 25%Cr steels, it was found that the diffusion rate of Mn was stronger than that of Cr [45]. In case of C, the formation of $M_{23}C_6$ is the governing driving force for C diffusion during the tempering step.

Structure and chemistry of precipitate phases

TEM characterizations of earlier batches of unirradiated EUROFER97 have been carried out for example by Klimenkov et al. [18] and Fernandez et al. [21]–[23]. Klimenkov et al. [18] found that in EUROFER four types of precipitates are present: $M_{23}C_6$, TaC, VN and TiN. Since our material the Ti content was minimal (see Table 1) all mentioned precipitates except TiN were observed. Fernandez et al. [23] additionally observed M_2X-type precipitates i.e., $Cr_2(C,N)$ in their material, which was also not observed in the current analysis. The precipitation behavior depends on the initial material composition and the applied heat treatment (see thermodynamics section above). Basically, the applied temperature and the Gibbs energy of each phase defines which phase will be preferentially formed, which was also mentioned by Klimenkov et al. [18]. The measured TEM data on the distribution of precipitates confirms the above-calculated precipitation sequence (Fig. 1) i.e., first TaC followed by VN and finally $M_{23}C_6$. In particular, TaC is randomly distributed in the martensite laths, because it is stable during the austenitization step, which is in our case also true for VN. As explained above the $M_{23}C_6$ precipitates are last to be formed at preferential sites such as PAGs and lath boundaries as can be seen for example in Fig. 3. Since the tempering step takes in our case is 2 h, there is some recrystallization of the martensitic laths to expected, which locally removes Fe-Cr matrix/precipitate orientation relationships. Our measured size distribution of $M_{23}C_6$ and MX-type particles is in accordance with that reported by Ferndandez et al. [21].

All observed precipitate phases have a face-centered cubic structure with lattice constants of 10.66 Å (ICSD No. 62667), 4.45 Å (ICSD No. 159875), and 4.13 Å (ICSD No. 22321) for $M_{23}C_6$, TaC and VN, respectively. Those values were used to index the selected area diffraction pattern as well as the Fast Fourier Transformed high-resolution phase contrast images and explain the occurring diffraction spots. Furthermore, the used crystal structures for both MX-type phases are in

accordance with those used by Klimenkov et al. [18]. Furthermore, in case of $M_{23}C_6$ a crystal defect was observed in one $M_{23}C_6$ precipitate on a (1 1 1) plane. This seems to be a common defect in these structures, since it is also observed in $M_{23}C_6$ precipitates being present in other type of steels as for example reported by Xu et al. [46]. In addition, they claim that the $M_{23}C_6$ phase has a close orientational relationship to the austenite phase. In our case, we were not able to establish a direct orientation relationship between martensite laths and neighboring $M_{23}C_6$ precipitate in some cases for example see Fig. 8 whereas in other region of the sample precipitates are aligned with a neighboring martensite grain as shown in Fig. 9. MX-type precipitates being attached to one another called a V-wing have an orientation relationship as can be seen in Fig. 10a and b with each other due to their origination. According to Fernandez et al. [21] V-wings have their origin in a spherical TaC particle on which a VN grows by secondary precipitation, which explains the orientational relationship.

The precipitates as well as the Fe-Cr matrix were analyzed by STEM-EDX. In the past, quantitative evaluation was hampered by mainly two factors: (i) only a handful of particles could be manually analyzed and (ii) often precipitate quantification results are distorted by matrix elements. For example in the work of Klimenkov et al. [18] the Fe content in the $M_{23}C_6$ phase is overestimated due to this problem. This can be circumvented by preparing carbon extraction replica in which the Fe-Cr matrix is etched away, and the precipitates are embedded into a carbon film being transferred onto a TEM grid. Then the metallic components in the sample can be quantified relatively accurate as can be seen in the work of Fernandez et al. [23]. However, at the same time it is not possible to quantify carbon in this kind of samples. Another recent publication by Cui et al. [16] deals with APT of EUROFER samples. The quantification results of the Fe-Cr matrix, the $M_{23}C_6$ and VN precipitates is comparable to our own STEM-EDX results. TaC as observed in our samples were not present or not detected in the samples of Cui et al. [16]. The elemental contents differ by a few at% between STEM-EDX and APT in the case of VN for V and N. However, there are differences between STEM-EDX and APT that affect the quantification results such as for example matrix-precipitate overlap in STEM-EDX datasets or limited precipitate statistics in APT samples. Furthermore, slightly different starting compositions and a different heat treatment may limit the accuracy of a direct comparison of our own results with the available literature data.

With the increase of computational power and the emergence of new fast acquisition spectrometers in the TEM world in the last decade, another way of analysis i.e., principal component analysis became possible. In our case it splits the STEM-EDX datasets acquired for example in standard EUROFER TEM samples into two new datasets containing the signal data in the form single EDX spectra and the navigation data i.e., elemental maps. The method is implemented among others in Hyperspy [26]. For the analysis of STEM-EDX or STEM-EELS data more physically interpretable datasets are desirable. The non-negative matrix factorization (NMF) algorithm provides exactly this functionality [31]. Fig. 6 contains results of such a NMF decomposition of STEM-EDX dataset acquired in EUROFER. Since NMF provides no negative peak intensities in the extracted spectra, they can be quantified if for example the k-factors of the system are known (see Table 5).

By comparing our results with those that were measured in replica samples as for example in the work of Fernandez et al. [23] as well as with the ThermoCalc predictions, it becomes evident that NMF overestimates matrix elements like Fe and Cr in precipitate EDX spectra quantifications. In addition, the Fe content of the Fe-Cr matrix is overestimated by a few at% whereas the Cr content is underestimated by about the same value as can be seen if the corresponding values in Table 2 are compared to those in Table 5. A similar behavior was observed during the evaluation of the $M_{23}C_6$ data. As can be seen by comparing Table 2 to Table 5 the Fe content is about 3x that of Cr in the NMF data whereas it should be only 2x as suggested by the ThermoCalc data in Table 2, which is in accordance with the data measured by

Fernandez et al. [23]. In case of the MX-type phases the obtained results are quite close to the predicted ones, however, surface contamination might hamper the results, especially in the quantification of C and N. Summarizing can be concluded that NMF in principle works, but if elements are present in both matrix and precipitate then there arise problems in separating those in a quantitatively correct way. As recently summarized by Kalinin et al. [47] PCA-based methods such as NMF can introduce artifacts compared to the raw data such as for example changes in peak intensities, which then result in wrong elemental contents.

Microstructural link to mechanical properties

Concerning the formation of structure–property relationships RAFM-type steels it is vital to link the obtained microstructural data to mechanical parameters such as for example yield strength and precipitate strengthening [48]. For the intended use in a high-temperature environment the MX-type but also the $M_{23}C_6$ particles play an important role in limiting grain growth by pinning the grain boundaries. According to Kozeschnik and Holzer [49] for microstructure-property relationships several interactions need to be considered among them precipitate-dislocation interaction and precipitate-(sub)grain boundary interaction. In order to estimate the strength of these interactions one needs to calculate for example the Orowan stress defining the precipitate-dislocation interaction, which itself is proportional to the shear modulus, magnitude of the Burgers vector and the average particle distance. Shear modulus and magnitude of the Burgers vector are both material constants whereas the average particle distance was determined above. In addition, according to Tan and Busby [50] also the morphology of the particles influence their influence on the materials strength. For example, spherical particles such as MX-type precipitates behave slightly different than rod- or platelet-shaped such as $M_{23}C_6$.

For the precipitate-(sub)grain boundary interaction Zener pinning is the relevant quantity as describes in [49]. Kozeschnik and Holzer [49] also stated that subgrains are the dominating quantity, since their number is much larger than for example those of the PAG. In case of martensite the martensitic laths can be used as first approximation. Then their grain size can be used to calculate their strength contribution, which is roughly inversely proportional to the square root of the grain size [49]. All aforementioned factors can be summed up in a single formula as for example carried out by Wang et al. [51] to model the yield strength of the material at hand.

Conclusions

Extensive analytical electron microscopical analyses were carried out from the micrometer scale down to the nanometer scale to characterize three variants of the 9% RAFM steel EUROFER97/3. No huge microstructural differences were observed between the three grades. SEM-EBSD was used to determine PAG and lath sizes of the martensite matrix. The PAG size varied between 4.5 µm and 6.5 µm. The Nishiyama-Wassermann reconstruction algorithm yields principally slightly larger PAG sizes compared to the Kurdjumov-Sachs based algorithm. Furthermore, the martensitic lath sizes determined by SEM-EBSD are only half or 1/3 of that determined manually from TEM images, which might be related to the limited statistics in this type of TEM data evaluations. The SEM-EDX shows that $M_{23}C_6$-type phases are preferentially located on lath and grain boundaries, which agrees with TEM-EDX measurements. The reason is preferential diffusion of elements like Cr, W, and C to and along grain boundaries. TEM methods like STEM-EDX and HRTEM were used to describe the occurring precipitates i.e., $M_{23}C_6$, VN, TaC morphologically, structurally, and chemically:

The average particle sizes for all analyzed EUROFER97/3 grades were 137–152 nm, 29–35 nm and 45–52 nm for $M_{23}C_6$, TaC, and VN, respectively.

The number densities are for all types of precipitates in the range in between 10^{19}-10^{20} particles per m^2.

The determined nearest neighbor distances of the $M_{23}C_6$ precipitates was found to lie in between 275 nm and 310 nm whereas for the MX-type phases (TaC and VN) the nearest neighbor is 124–176 nm away.

TEM diffraction data evaluation confirms that $M_{23}C_6$, TaC and VN fit to the database structures ICSD No. 62667, ICSD No. 159875, and ICSD No. 22321, respectively. The matrix is described by ferrite ICSD No. 52258 since the martensitic distortion is not resolved by TEM diffraction methods.

In addition, the thermodynamic calculations were carried out to explain phase formation, phase fraction and phase composition. The results are in good agreement with the experimentally determined values. These results will provide a good basis to explain the mechanical performance of these materials as it was discussed in the last part. It will also set a good comparison reference for the neutron-irradiated material.

Declaration of Competing Interest

The authors declare that they have no known competing financial interests or personal relationships that could have appeared to influence the work reported in this paper.

Data availability

Data will be made available on request.

References

[1] G. Aiello, J. Aktaa, F. Cismondi, G. Rampal, J.-F. Salavy, F. Tavassoli, Assessment of design limits and criteria requirements for Eurofer structures in TBM components, J. Nucl. Mater. 414 (1) (Jul. 2011) 53–68, https://doi.org/10.1016/j.jnucmat.2011.05.005.

[2] G.R. Odette, M.J. Alinger, B.D. Wirth, Recent developments in irradiation-resistant steels, Annu. Rev. Mat. Res. 38 (1) (2008) 471–503, https://doi.org/10.1146/annurev.matsci.38.060407.130315.

[3] C.C. Eiselt, et al., ODS-materials for high temperature applications in advanced nuclear systems, Nucl. Mater. Energy 9 (Dec. 2016) 22–28, https://doi.org/10.1016/j.nme.2016.08.017.

[4] I. Hilger, et al., Fabrication and characterization of oxide dispersion strengthened (ODS) 14Cr steels consolidated by means of hot isostatic pressing, hot extrusion and spark plasma sintering, J. Nucl. Mater. 472 (Apr. 2016) 206–214, https://doi.org/10.1016/j.jnucmat.2015.09.036.

[5] M. Rieth, et al., Technological processes for steel applications in nuclear fusion, Appl. Sci. 11 (24) (Jan. 2021), https://doi.org/10.3390/app112411653. Art. no. 24.

[6] K. Ehrlich, S. Kelzenberg, H.-D. Röhrig, L. Schäfer, M. Schirra, The development of ferritic-martensitic steels with reduced long-term activation, J. Nucl. Mater. 212–215 (Sep. 1994) 678–683, https://doi.org/10.1016/0022-3115(94)90144-9.

[7] M.R. Gilbert, J.-C. Sublet, Handbook of activation, transmutation, and radiation damage properties of the elements simulated using FISPACT-II & TENDL-2015; Magnetic Fusion Plants, p. 785.

[8] M. Zmitko, et al., The European ITER Test Blanket Modules: EUROFER97 material and TBM's fabrication technologies development and qualification, Fusion Eng. Des. 124 (Nov. 2017) 767–773, https://doi.org/10.1016/j.fusengdes.2017.04.051.

[9] M. Ayada, M. Yuga, N. Tsuji, Y. Saito, A. Yoneguti, Effect of vanadium and niobium on restoration behavior after hot deformation in medium carbon spring steels, ISIJ Int. 38 (9) (1998) 1022–1031, https://doi.org/10.2355/isijinternational.38.1022.

[10] C. Dethloff, E. Gaganidze, J. Aktaa, Quantitative TEM analysis of precipitation and grain boundary segregation in neutron irradiated EUROFER97, J. Nucl. Mater. 454 (1) (Nov. 2014) 323–331, https://doi.org/10.1016/j.jnucmat.2014.07.078.

[11] C. Dethloff, E. Gaganidze, J. Aktaa, Microstructural defects in EUROFER 97 after different neutron irradiation conditions, Nucl. Mater. Energy 9 (Dec. 2016) 471–475, https://doi.org/10.1016/j.nme.2016.05.009.

[12] M. Klimenkov, P. Vladimirov, A. Möslang, E. Materna-Morris, H.-C. Schneider, TEM study of irradiation induced copper precipitation in boron alloyed EUROFER97 steel: Dedicated to Prof. Dr.-Ing. Heinrich Wollenberger on the occasion of his 80th birthday, Int. J. Mater. Res. 102 (9) (Sep. 2011) 1089–1093, https://doi.org/10.3139/146.110570.

[13] M. Klimenkov, A. Möslang, E. Materna-Morris, Helium influence on the microstructure and swelling of 9%Cr ferritic steel after neutron irradiation to 16.3dpa, J. Nucl. Mater. 453 (1) (Oct. 2014) 54–59, https://doi.org/10.1016/j.jnucmat.2014.05.001.

[14] M. Klimenkov, E. Materna-Morris, A. Möslang, Characterization of radiation induced defects in EUROFER 97 after neutron irradiation, J. Nucl. Mater. 417 (1) (Oct. 2011) 124–126, https://doi.org/10.1016/j.jnucmat.2010.12.261.

[15] J. Hoffmann, M. Rieth, M. Klimenkov, S. Baumgärtner, Improvement of EUROFER's mechanical properties by optimized chemical compositions and thermo-mechanical treatments, Nucl. Mater. Energy 16 (Aug. 2018) 88–94, https://doi.org/10.1016/j.nme.2018.05.028.

[16] L. Cui, Y. Dai, S.S.A. Gerstl, M.A. Pounchon, APT characterization of irradiation effects on MX phase in reduced-activation ferritic/martensitic steels, J. Nucl. Mater. 573 (Jan. 2023), 154121, https://doi.org/10.1016/j.jnucmat.2022.154121.

[17] G. Yeli, V.C.I. Strutt, M.A. Auger, P.A.J. Bagot, M.P. Moody, Characterisation of nano-scale precipitates in BOR60 irradiated T91 steel using atom probe tomography, J. Nucl. Mater. 543 (Jan. 2021), 152466, https://doi.org/10.1016/j.jnucmat.2020.152466.

[18] M. Klimenkov, R. Lindau, E. Materna-Morris, A. Möslang, TEM characterization of precipitates in EUROFER 97, Prog. Nucl. Energy 57 (May 2012) 8–13, https://doi.org/10.1016/j.pnucene.2011.10.006.

[19] S. Kano, et al., Investigation of instability of $M_{23}C_6$ particles in F82H steel under electron and ion irradiation conditions, J. Nucl. Mater. 502 (Apr. 2018) 263–269, https://doi.org/10.1016/j.jnucmat.2018.02.004.

[20] V.M. Chernov, et al., Thermal stability of the microstructure of 12% chromium ferritic–martensitic steels after long-term aging at high temperatures, Tech. Phys. 61 (2) (Feb. 2016) 209–214, https://doi.org/10.1134/S1063784216020092.

[21] P. Fernández, A.M. Lancha, J. Lapeña, M. Serrano, M. Hernández-Mayoral, Metallurgical properties of reduced activation martensite steel Eurofer'97 in the as-received condition and after thermal ageing, J. Nucl. Mater. 307–311 (Dec. 2002) 495–499, https://doi.org/10.1016/S0022-3115(02)01013-9.

[22] P. Fernández, M. García-Mazarío, A.M. Lancha, J. Lapeña, Grain boundary microchemistry and metallurgical characterization of Eurofer'97 after simulated service conditions, J. Nucl. Mater., 329–333 (Aug. 2004) 273–277, 10.1016/j.jnucmat.2004.04.055.

[23] P. Fernández, J. Hoffmann, M. Rieth, A. Gómez-Herrero, Microstructure and precipitation behavior of advanced RAFM steels for high-temperature applications on fusion reactors, Mater. Charact. 180 (Oct. 2021) 111443, https://doi.org/10.1016/j.matchar.2021.111443.

[24] G. Lucas, P. Burdet, M. Cantoni, C. Hébert, Multivariate statistical analysis as a tool for the segmentation of 3D spectral data, Micron 52–53 (Sep. 2013) 49–56, https://doi.org/10.1016/j.micron.2013.08.005.

[25] D. Rossouw, et al., Multicomponent signal unmixing from nanoheterostructures: overcoming the traditional challenges of nanoscale X-ray analysis via machine learning, Nano Lett. 15 (4) (Apr. 2015) 2716–2720, https://doi.org/10.1021/acs.nanolett.5b00449.

[26] F. de la Peña, et al., hyperspy/hyperspy: Release v1.7.2, Zenodo (Sep. 18, 2022), https://doi.org/10.5281/zenodo.7090040.

[27] D.C. Palmer, S.E. Palmer, SingleCrystal^{TM}: a single-crystal diffraction program for Mac and Windows. CrystalMaker Software Ltd., Oxford. [Windows, MacOS]. www.crystalmaker.com.

[28] F. Niessen, T. Nyyssönen, A.A. Gazder, R. Hielscher, Parent grain reconstruction from partially or fully transformed microstructures in MTEX, J. Appl. Cryst. 55 (1) (Feb. 2022), https://doi.org/10.1107/S1600576721011560. Art. no. 1.

[29] A. Tripathi, S. Zaefferer, On the resolution of EBSD across atomic density and accelerating voltage with a particular focus on the light metal magnesium, Ultramicroscopy 207 (Dec. 2019), 112828, https://doi.org/10.1016/j.ultramic.2019.112828.

[30] M.R. Keenan, P.G. Kotula, Accounting for Poisson noise in the multivariate analysis of ToF-SIMS spectrum images, Surf. Interface Anal. 36 (3) (2004) 203–212, https://doi.org/10.1002/sia.1657.

[31] O. Nicoletti, F. de la Peña, R.K. Leary, D.J. Holland, C. Ducati, P. A. Midgley, Three-dimensional imaging of localized surface plasmon resonances of metal nanoparticles, Nature, 502(7469) (Oct. 2013), 10.1038/nature12469 (Art. no. 7469).

[32] C.S. Roberts, Effect of carbon on the volume fractions and lattice parameters of retained austenite and martensite, JOM 5 (2) (Feb. 1953) 203–204, https://doi.org/10.1007/BF03397477.

[33] F. Abe, M. Taneike, K. Sawada, Alloy design of creep resistant 9Cr steel using a dispersion of nano-sized carbonitrides, Int. J. Press. Vessel. Pip. 84 (1) (Jan. 2007) 3–12, https://doi.org/10.1016/j.ijpvp.2006.09.003.

[34] C.A. Danon, C. Servant, Thermodynamic modeling in reduced activation steels, ISIJ Int. 45 (6) (2005) 903–912, https://doi.org/10.2355/isijinternational.45.903.

[35] V.B. Oliveira, K.D. Zilnyk, H.R.Z. Sandim, Thermodynamic simulation of reduced activation ferritic–martensitic Eurofer-97 steel, J. Phase Equilib. Diffus. 38 (3) (Jun. 2017) 208–216, https://doi.org/10.1007/s11669-017-0530-2.

[36] O. Kachko, A. Puype, D. Terentyev, G. Bonny, W.V. Renterghem, R.H. Petrov, Development of RAFM steels for high temperature applications guided by thermodynamic modelling, Nucl. Mater. Energy 32 (Sep. 2022), 101211, https://doi.org/10.1016/j.nme.2022.101211.

[37] M. Hillert, B. Sundman, B. Jansson, Ågren, Computational Materials Engineering, Thermo-Calc Software. https://thermocalc.com/ (accessed Oct. 21, 2022).

[38] S.-L. Chen, et al., The PANDAT software package and its applications, Calphad 26 (2) (Jun. 2002) 175–188, https://doi.org/10.1016/S0364-5916(02)00034-2.

[39] T. Gräning, N. Sridharan, Benchmarking a 9Cr-2WVTa reduced activation ferritic martensitic steel fabricated via additive manufacturing, Metals 12(2) (Feb. 2022), 10.3390/met12020342 (Art. no. 2).

[40] R.L. Klueh, D.R. Harries, High-Chromium Ferritic and Martensitic Steels for Nuclear Applications, Astm Intl., W. Conshohocken, PA, 2001.

[41] S.R. Shatynski, The thermochemistry of transition metal carbides, Oxid. Met. 13 (2) (Apr. 1979) 105–118, https://doi.org/10.1007/BF00611975.

[42] D.R. Sigler, Aluminum oxide adherence on Fe-Cr-Al alloys modified with group IIIB, IVB, VB, and VIB elements, Oxid. Met. 32 (5) (Dec. 1989) 337–355, https://doi.org/10.1007/BF00665442.

[43] P. Fernández, M. García-Mazarío, A.M. Lancha, J. Lapeña, Grain boundary microchemistry and metallurgical characterization of Eurofer'97 after simulated service conditions, J. Nucl. Mater., 329–333 (Aug. 2004) 273–277, 10.1016/j.jnucmat.2004.04.055.

[44] J. Askill, Tracer Diffusion Data for Metals, Alloys, and Simple Oxides. Springer US, Boston, MA, 1970. 10.1007/978-1-4684-6075-9.

[45] W.-T. Wu, Y.-S. Zhang, W.-H. Wang, K. Li, S.-W. Du, W. Yang, Mn diffusion in the ferritic Fe-25 %Cr alloy: A first-principles study, Mater. Sci. Eng.: B 286 (Dec. 2022), 116042, https://doi.org/10.1016/j.mseb.2022.116042.

[46] Z. Xu, Z. Ding, L. Dong, B. Liang, Characterization of $M_{23}C_6$ carbides precipitating at grain boundaries in 100Mn13 steel, Metall. Mater. Trans. A 47 (10) (Oct. 2016) 4862–4868, https://doi.org/10.1007/s11661-016-3656-7.

[47] S.V. Kalinin et al., Machine learning in scanning transmission electron microscopy, Nat. Rev. Methods Primers 2(1) (Mar. 2022), 10.1038/s43586-022-00095-w (Art. no. 1).

[48] K. Maruyama, K. Sawada, J. Koike, Strengthening mechanisms of creep resistant tempered martensitic steel, ISIJ Int. 41 (6) (2001) 641–653, https://doi.org/10.2355/isijinternational.41.641.

[49] E. Kozeschnik, I. Holzer, 10 - Precipitation during heat treatment and service: characterization, simulation and strength contribution, in: F. Abe, T.-U. Kern, R. Viswanathan (Eds.), Creep-Resistant Steels, in Woodhead Publishing Series in Metals and Surface Engineering. Woodhead Publishing, 2008, pp. 305–328. 10.1533/9781845694012.2.305.

[50] L. Tan, J.T. Busby, Formulating the strength factor α for improved predictability of radiation hardening, J. Nucl. Mater. 465 (Oct. 2015) 724–730, https://doi.org/10.1016/j.jnucmat.2015.07.009.

[51] C. Wang, C. Zhang, Z. Yang, J. Zhao, Multiscale simulation of yield strength in reduced-activation ferritic/martensitic steel, Nucl. Eng. Technol. 49 (3) (Apr. 2017) 569–575, https://doi.org/10.1016/j.net.2016.10.006.